

Supplementary information

Electroreduction of NO_3^- on tubular porous Ti electrodes

Piotr M. Krzywda^{a,b}, Ainoa Paradelo Rodríguez^a, Lukas Cino^a, Nieck E. Benes^b, Bastian T. Mei^a,

Guido Mul^{a,*}

^a Photocatalytic Synthesis Group, Faculty of Science & Technology of the University of Twente,
PO Box 217, Enschede, The Netherlands.

^b Membrane Science and Technology Cluster, Faculty of Science & Technology of the University of
Twente, PO Box 217, Enschede, The Netherlands.

* Corresponding author. E-mail address: g.mul@utwente.nl

Materials

Titanium powder (TLS Technik GmbH & Co., ASTM, grade 2) with an average particle size of 6 μm , polyethersulfone (PES, BASF, Ultrason E 6020P), and N-methylpyrrolidone (NMP, Sigma Aldrich, $\geq 99\%$) were used for Ti hollow fiber preparation. HClO_4 (Sigma Aldrich, 70 %) and KClO_4 (Sigma Aldrich, $\geq 99\%$) were used for preparation of the supporting electrolyte. KNO_3 (Sigma Aldrich, $\geq 99.0\%$) was used as NO_3^- source. Ammonium chloride (Alfa Aesar, 99.999 %), maleic acid (Sigma Aldrich, $\geq 99\%$), DMSO-d₆ (Sigma Aldrich, 99.5 atom % D), hydroxylamine hydrochloride (Sigma Aldrich, 99.995%), acetone (Sigma Aldrich, 99.5%) and methanol (Sigma Aldrich, $\geq 99.9\%$) were used for product detection and calibration. Silver epoxy glue (Chemtronics, CW2400) and two-component adhesive glue (Weicon, 10550024) were used to prepare the electrode assembly.

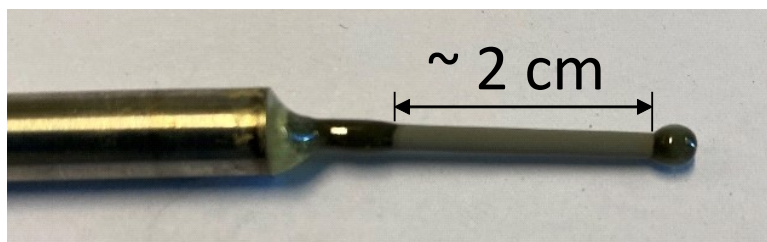


Figure S1. Photograph of a Ti hollow fiber electrode assembly.

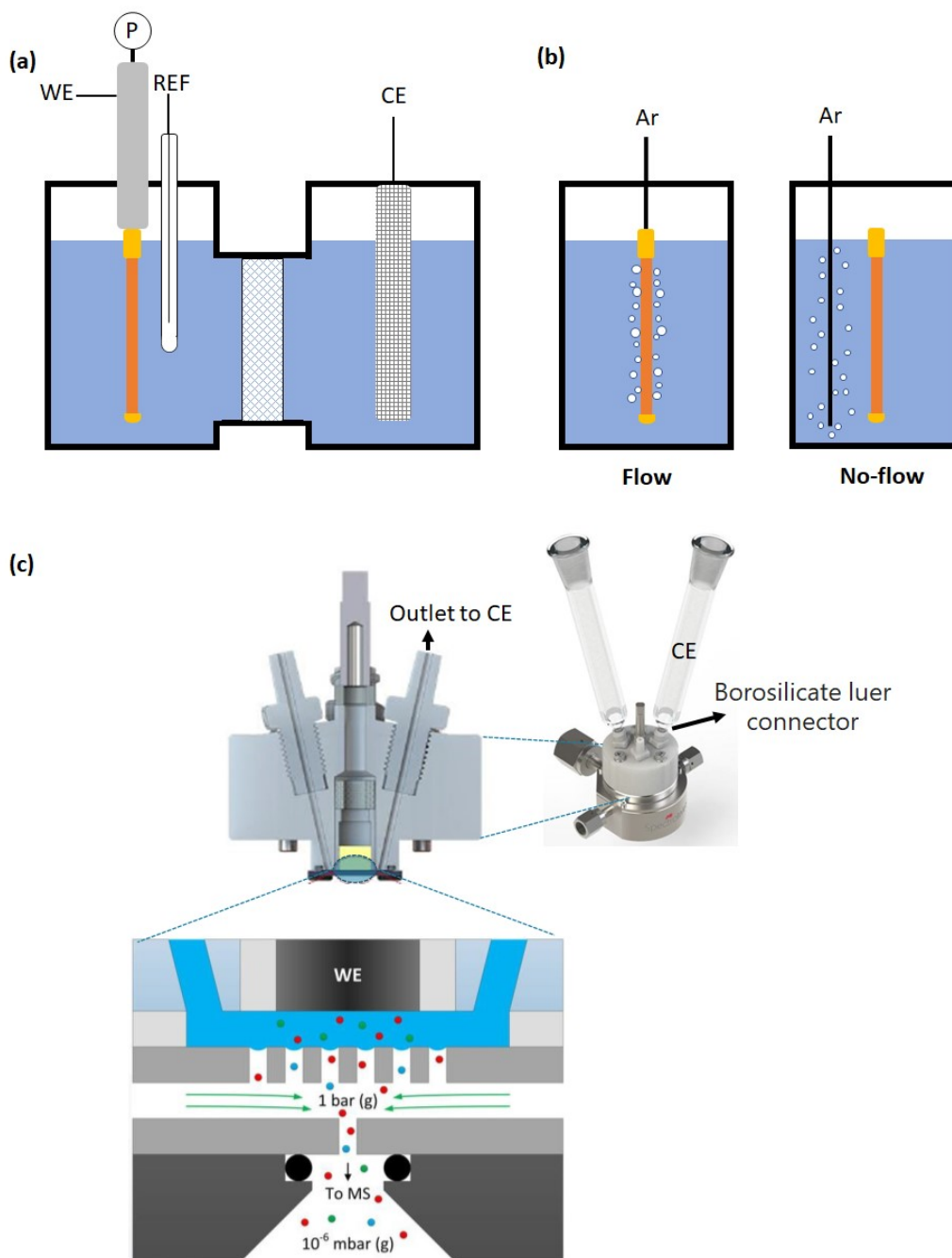


Figure S2. Schematic representation of (a) the applied electrochemical cell; (b) gas flow configurations of the working electrode compartment, and (c) the EC-MS set-up, and principle of the chip technology provided by Spectrolnlets.

Ammonia quantification

The concentration of ammonia was determined by ^1H NMR spectroscopy based on methods described elsewhere¹². Calibration was performed using standard NH_4Cl solutions with known concentration. Generally, 0.5 ml of the (standard) solution was mixed with 50 μl of 0.5 M H_2SO_4 containing 10 mM maleic acid (internal standard) and 25 μl of DMSO-d_6 as solvent. ^1H NMR spectra were recorded on a Bruker 400MHz spectrometer with 1000 scans (Figure S3). The area ratio of the NH_4^+ peak at 6.79 ppm and the maleic acid peak at 6.22 ppm were plotted versus NH_3 concentration (Figure S3).

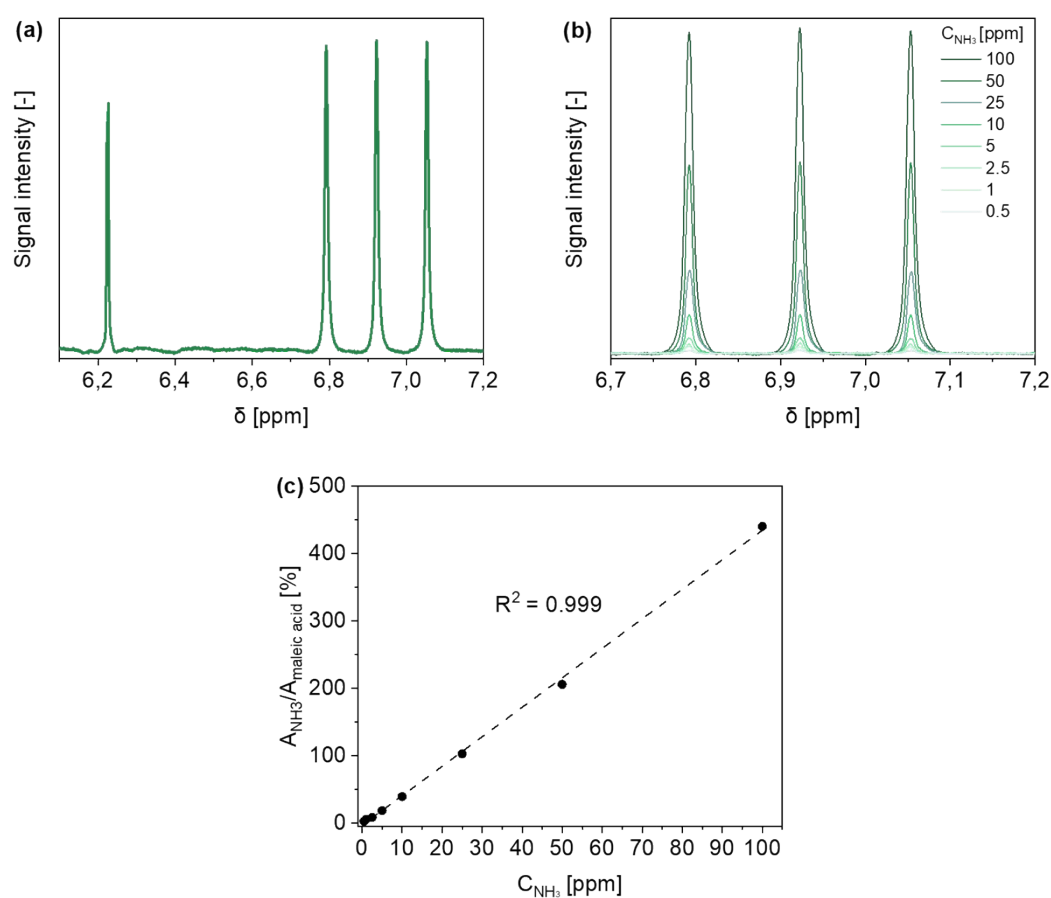


Figure S3. ^1H NMR spectrum of (a) 50 ppm NH_4^+ with 10 mM maleic acid and (b) different concentrations of NH_4^+ . (c) Calibration curve for NH_4^+ quantification.

Hydroxylamine quantification

The hydroxylamine content was determined by gas chromatography according to a method published elsewhere³. In short, samples obtained after electrolysis were neutralized by the addition of a NaOH solution. To allow for quantification, hydroxylamine was reacted with acetone to form acetone oxime by the addition of 2 μl of methanol/acetone (1:1 v/v) to 4 ml of the neutralized sample solution. Acetone oxime was quantitatively detected by gas chromatography (GC-FID, Figure S4). Following the procedures described above, the calibration curve was prepared using standard solutions of hydroxylamine hydrochloride (Figure S4).

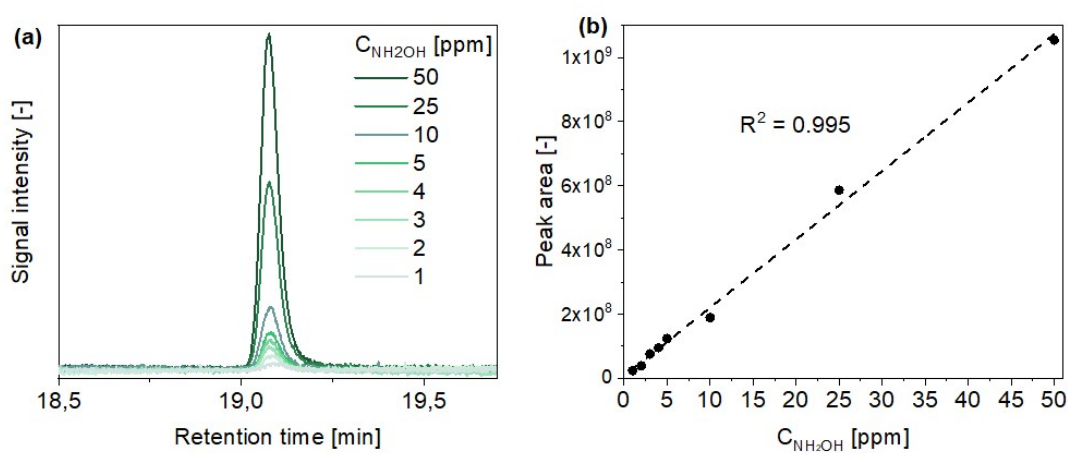


Figure S4. (a) Chromatogram (GC-FID) of NH_2OH with different concentration. (b) Calibration curve for NH_2OH quantification.

Nitrite quantification

The concentration of NO_2^- was determined using the commercial Spectroquant® Nitrite test (Supelco), where nitrite ions react with sulfanilic acid to form a diazonium salt, which then reacts with N-(1-naphthyl)ethylenediamine dihydrochloride to form a red-violet azo dye. Generally, the electrolyte solution was mixed with 0.1 M NaOH (to achieve the required pH range) and 1 microspoon of reagent. After the reagent was dissolved, the reaction mixture was left for 10 min and absorption at 520 nm was measured by UV-Vis spectroscopy. Following the procedure described above, the calibration curve was prepared using standard solutions of KNO_2 (Figure S5).

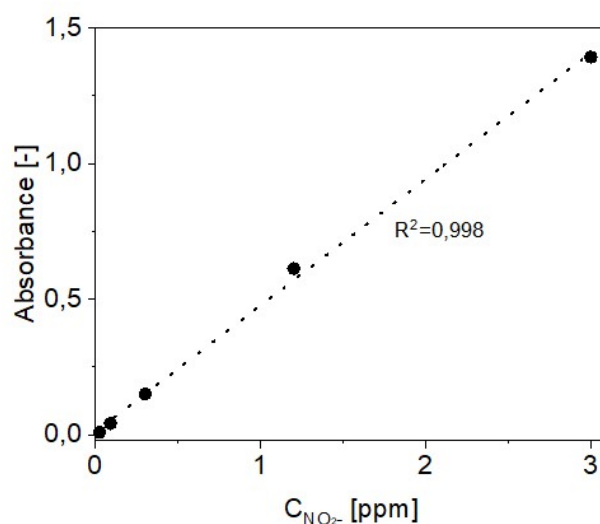


Figure S5. Calibration curve for NO_2^- quantification by UV-Vis spectroscopy.

Table S1. Standard reduction potentials of NO_3^- electroreduction reactions.

Reaction	E^0 [V vs RHE]
$\text{NO}_3^- + 2\text{H}^+ + e^- \rightarrow \text{NO}_2 + \text{H}_2\text{O}$	0.77
$\text{NO}_3^- + 2\text{H}^+ + 2e^- \rightarrow \text{NO}_2^- + \text{H}_2\text{O}$	0.94
$\text{NO}_3^- + 4\text{H}^+ + 3e^- \rightarrow \text{NO} + 2\text{H}_2\text{O}$	0.96
$2\text{NO}_3^- + 10\text{H}^+ + 8e^- \rightarrow \text{N}_2\text{O} + 5\text{H}_2\text{O}$	1.12
$2\text{NO}_3^- + 12\text{H}^+ + 10e^- \rightarrow \text{N}_2 + 6\text{H}_2\text{O}$	1.25
$\text{NO}_3^- + 7\text{H}^+ + 6e^- \rightarrow \text{NH}_2\text{OH} + 2\text{H}_2\text{O}$	0.73
$2\text{NO}_3^- + 16\text{H}^+ + 14e^- \rightarrow \text{N}_2\text{H}_4 + 6\text{H}_2\text{O}$	0.82
$\text{NO}_3^- + 9\text{H}^+ + 8e^- \rightarrow \text{NH}_3 + 3\text{H}_2\text{O}$	0.88

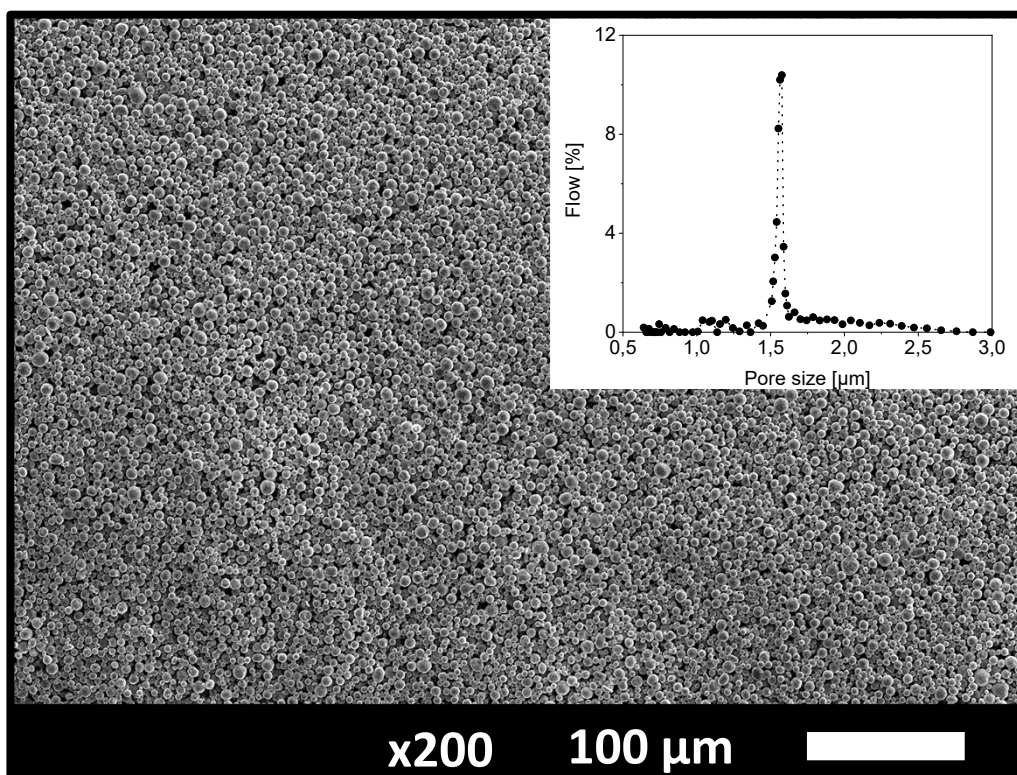


Figure S6. SEM image of the Ti hollow fiber wall with pore size distribution (see insert).

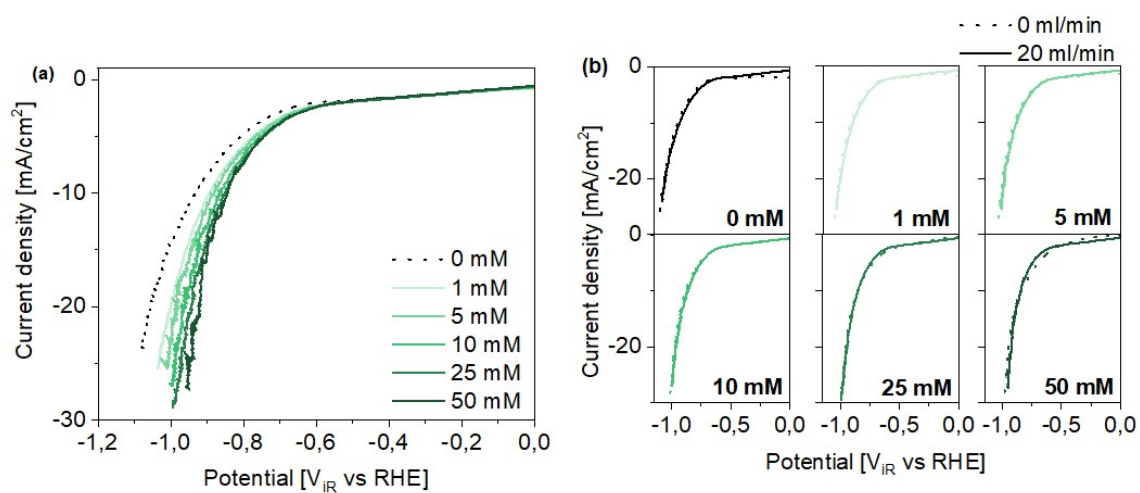


Figure S7. Linear scan voltammetry of a Ti hollow fiber in **neutral** pH electrolyte with (a) increasing KNO_3 concentration in the 'no-flow' configuration (see Fig S2), and (b) applying an Ar flow rate through the electrode

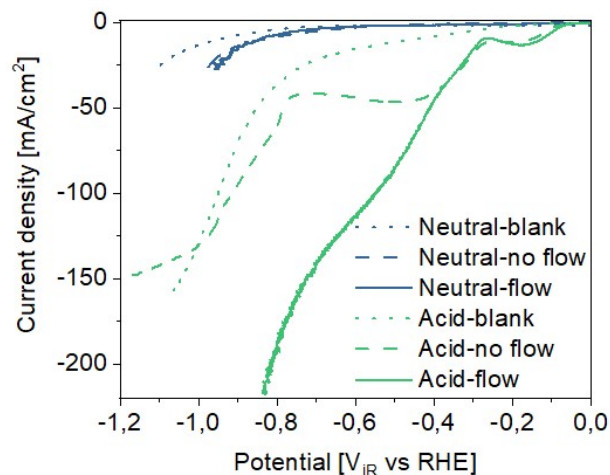


Figure S8. Comparison of the activity of the Ti hollow fiber electrode for NO_3^- electroreduction in acidic and neutral pH electrolyte, based on linear scan voltammetry.

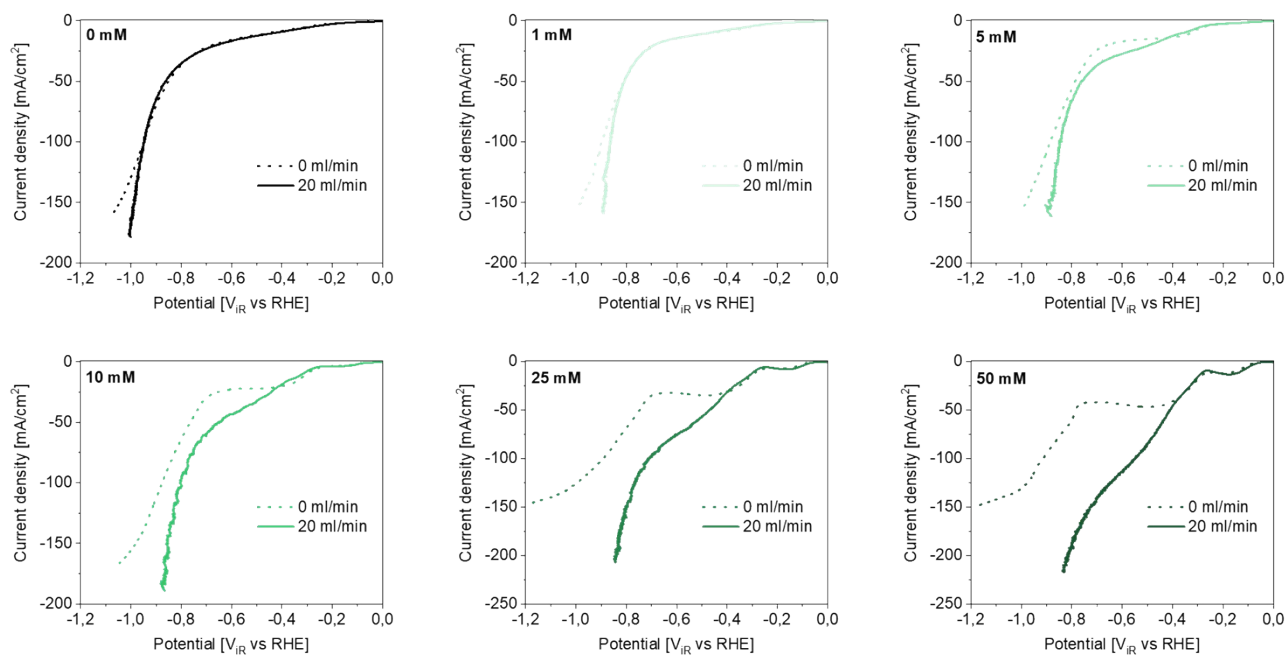


Figure S9. ‘No-flow’ vs flow at different nitrate concentrations, showing flow has a significant effect at concentrations larger than ~ 5 mM.

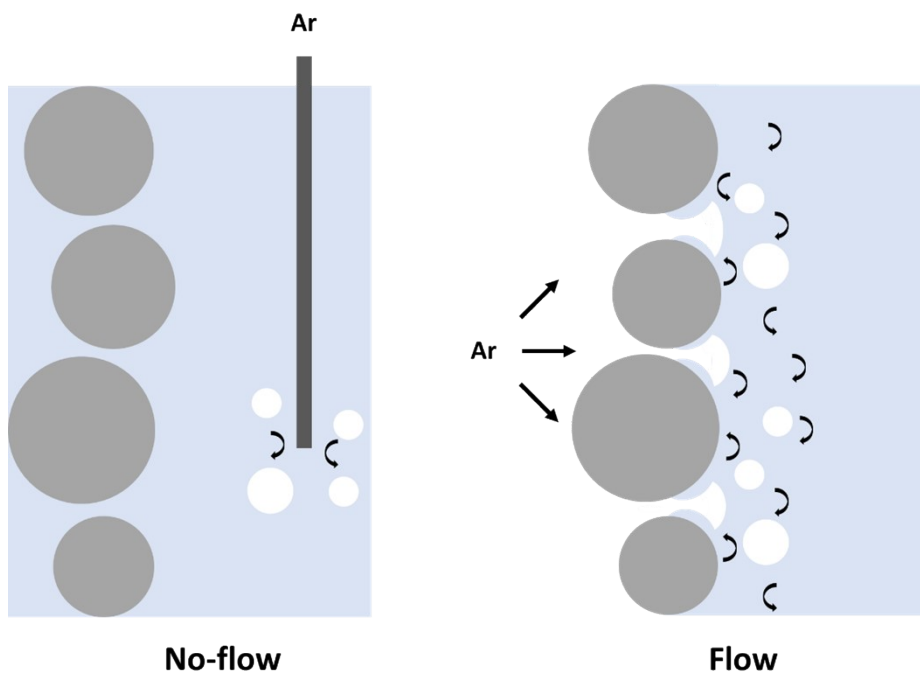


Figure S10. Schematic representation of the mixing effect induced by gas bubbles exiting the pores of the hollow fiber electrode (right), compared to a traditional configuration sparging the Ar gas in the vicinity of the fiber (left).

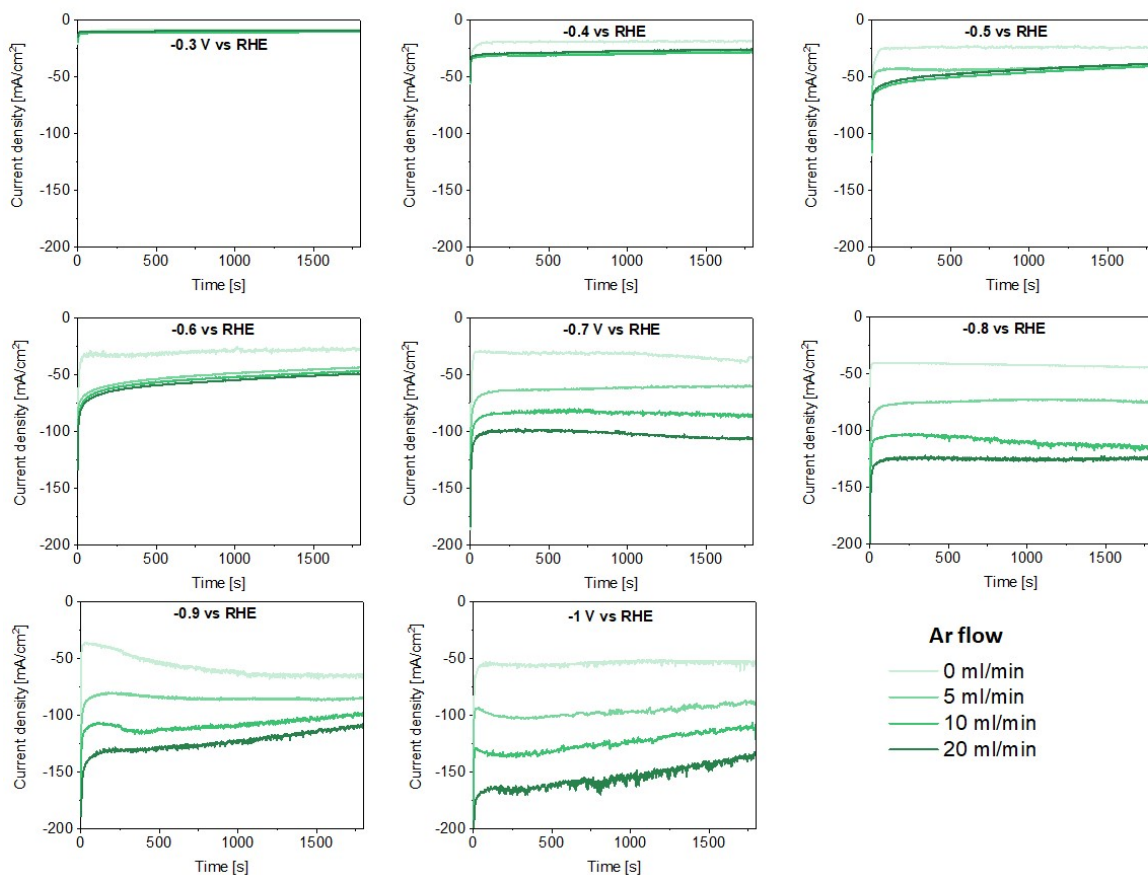


Figure S11. Measured current density during chronoamperometry at different potentials. The Ar flow rate strongly affects the current density at voltages > -0.8 V.

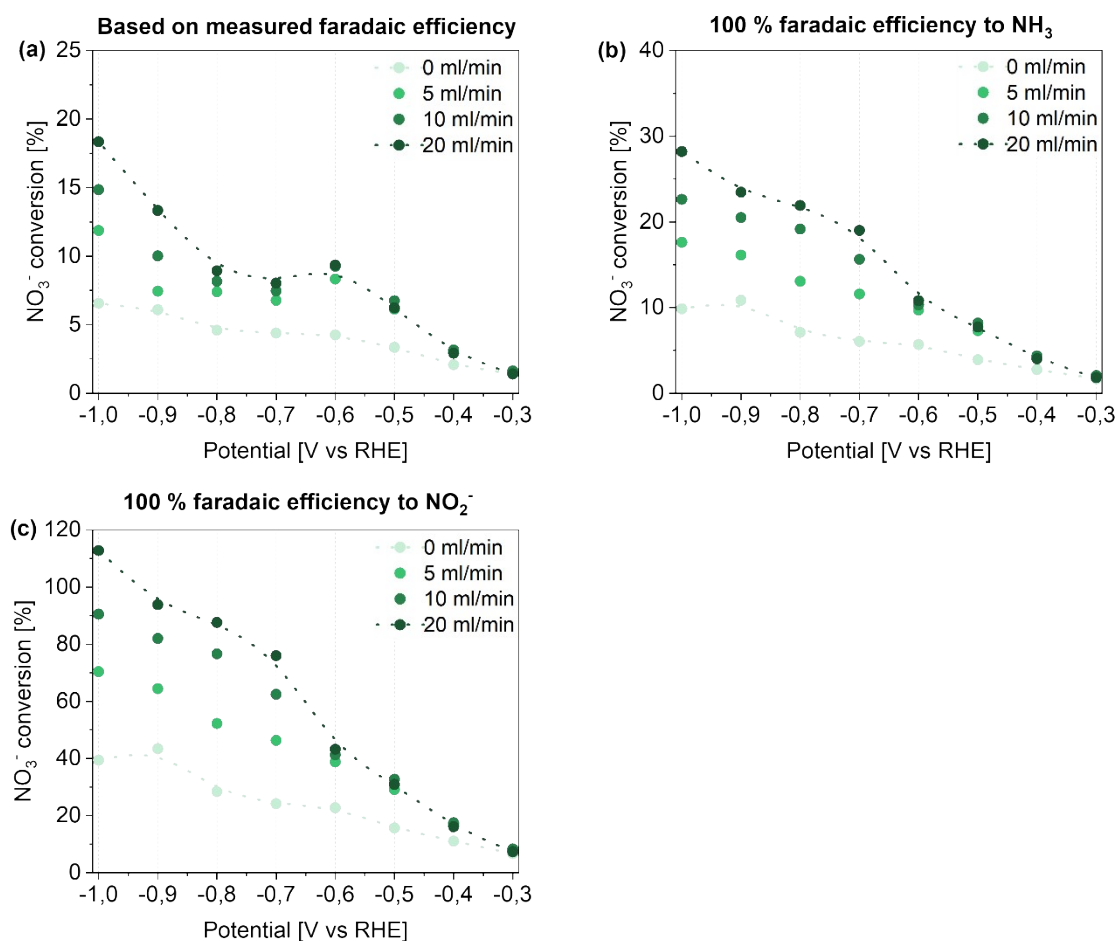


Figure S12. NO_3^- conversion depending on the applied potential and the Ar flow rate, calculated based on (a) the measured faradaic efficiency, (b) the assumption of 100 % faradaic efficiency to NH_3 and (c) the assumption of 100 % faradaic efficiency to NO_2^- .

The total charge passed during electrolysis was used in calculations of NO_3^- conversion. In Figure S11a, the measured faradaic efficiency to each product was used for calculation. Note that in addition to the proton-coupled electrochemical reactions, also decomposition of products might occur (as discussed in the main article). Thus, the real NO_3^- conversion is likely higher than presented by the estimations used. We assume 100 % faradaic efficiency to either ammonia (Figure S11b) or nitrite (Figure S11c). As evident, especially in the case of NO_2^- formation, a nitrate conversion close to 100 % be obtained. Most importantly NO_3^- conversion values calculated here are convincingly showing that depletion of the reactant in the electrolyte can influence the current density, especially at more negative potentials, and higher gas flow rates.

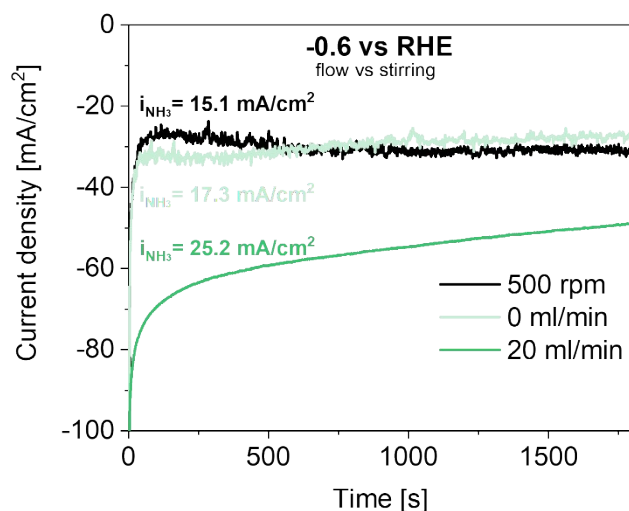


Figure S13. Current density during chronoamperometry at -0.6 V vs RHE in no flow (0 ml/min) and flow (20 ml/min) configuration compared to electrolyte stirred with 500 rpm.

An experiment with magnetic stirring was performed to reveal the improvement of bubble-induced mixing compared to the traditional way of convective mixing. As shown, a similar current density and partial current density to ammonium was observed in chronoamperometry at -0.6 V vs RHE in 50 mM KNO_3 acidic electrolyte using no-flow configuration and additional stirring at 500 rpm. It proves that even in a no-flow configuration, gas bubbles (supplied next to the electrode rather than through) provide similar convection in the system like stirring with 500 rpm. Most importantly, the result shows big improvement when gas is supplied through the electrode which creates more efficient mixing closer to the electrode surface.

Table S2. Measured iR drop before each chronoamperometry experiment.

iR drop [Ω] – 80% compensation				
Potential [V vs RHE]	Flow [ml/min]			
	0	5	10	20
-0.3	3.433	3.664	3.735	5.291
-0.4	5.087	5.515	5.521	5.953
-0.5	4.161	3.903	3.910	4.167
-0.6	5.856	5.270	4.961	5.203
-0.7	3.447	3.832	3.420	3.528
-0.8	3.400	3.425	3.520	4.024
-0.9	5.070	5.403	5.841	5.999
-1.0	4.055	3.869	3.476	3.573

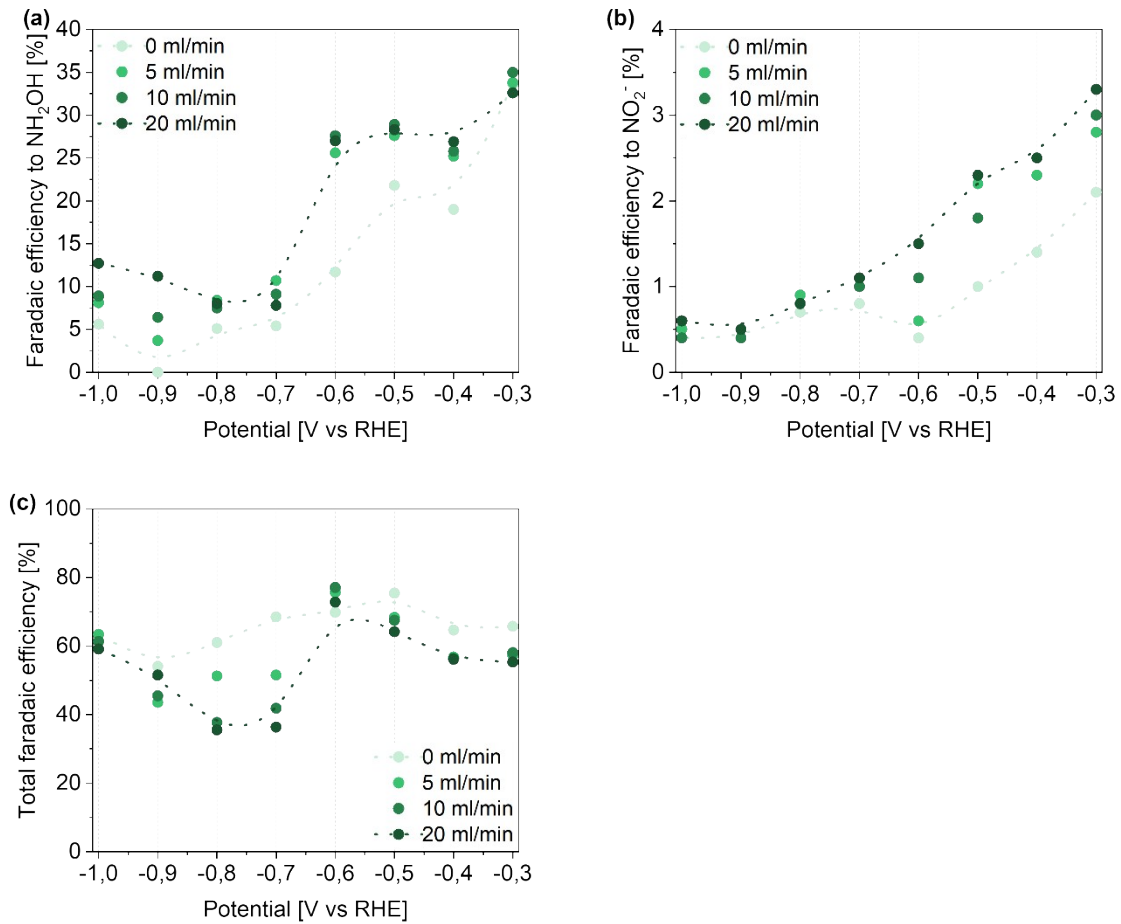


Figure S14. Faradaic efficiency to (a) NH_2OH , (b) NO_2^- and (c) total faradaic efficiency including NH_3 depending on applied potential and Ar flow rate.

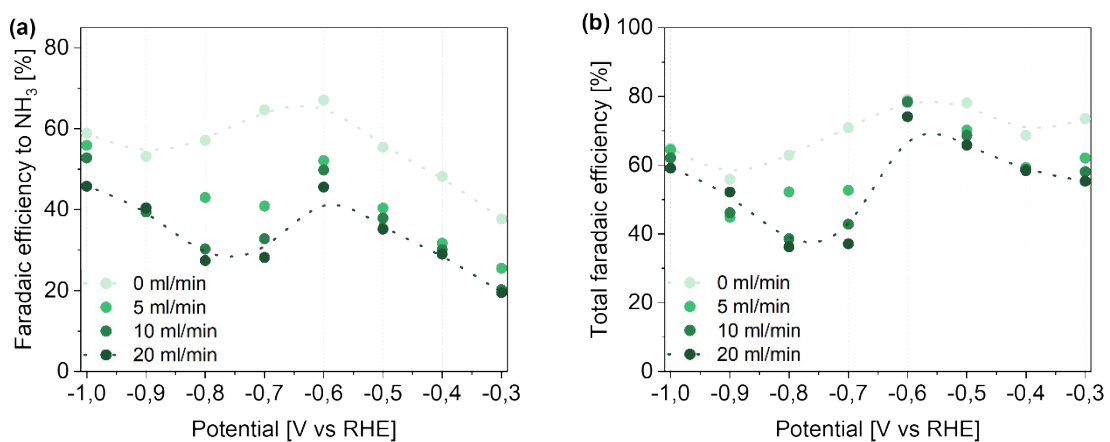


Figure S15. Faradaic efficiency to (a) NH_3 and (b) total faradaic efficiency including ammonia measured in the anodic compartment.

Since ammonia (NH_4^+ in acid) can cross the nafion membrane, its concentration was also measured in the counter electrode (CE) compartment of the electrolytic cell. However, due to the low concentration measured in the CE compartment, the accuracy of the measurement can be questionable due to

possible contaminations with ambient ammonia (common in the nitrogen electroreduction field). The data presented in the main text of the manuscript only include ammonia detected in the working electrode compartment.

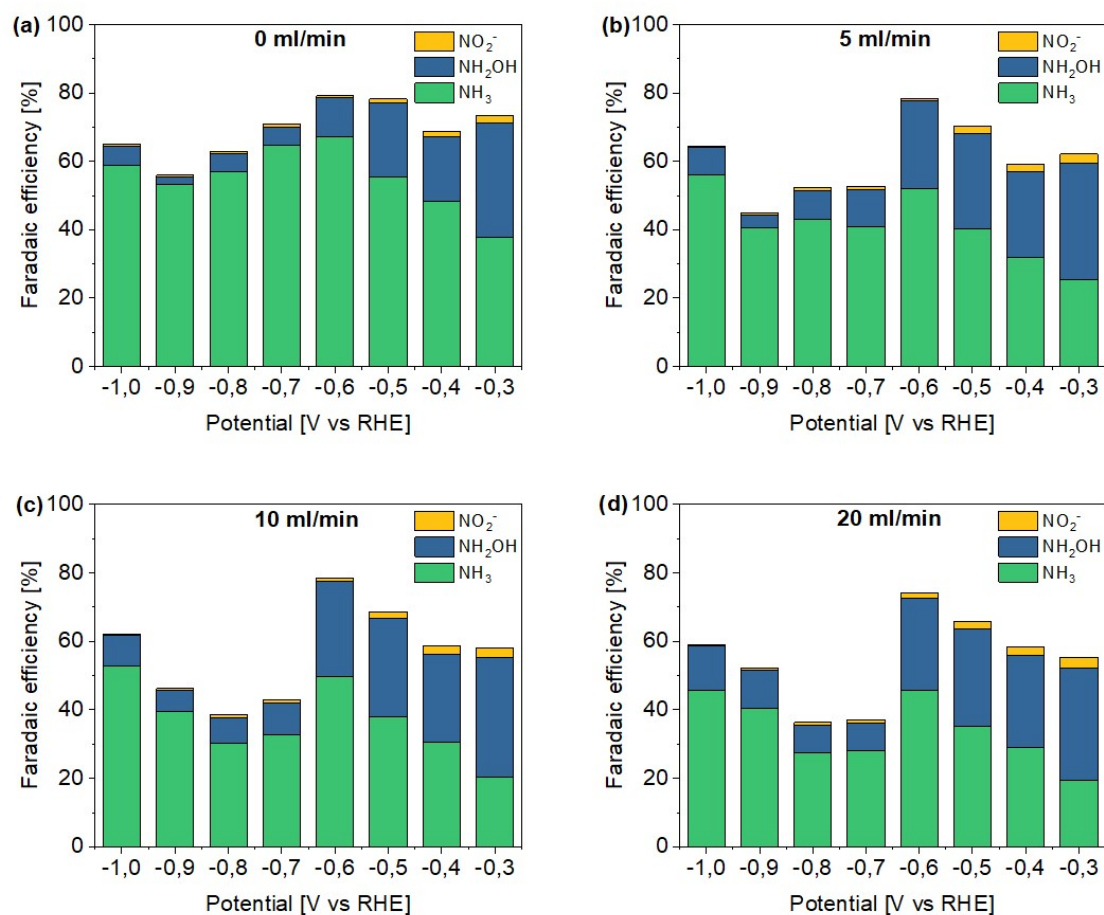


Figure S16. Total faradaic efficiency at different Ar flow rates including ammonia measured in the counter electrode compartment.

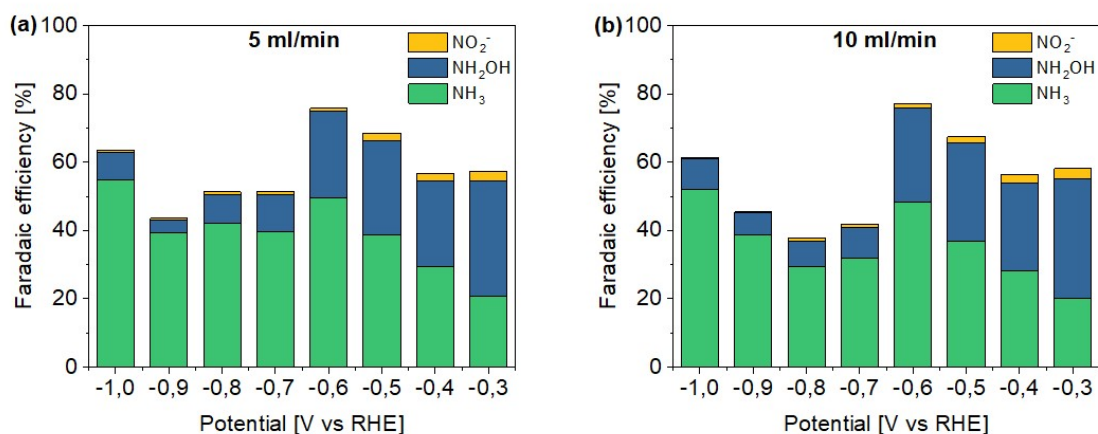


Figure S17. Total faradaic efficiency in flow configuration at (a) 5 ml/min and (b) 10 ml/min Ar flow.

Faradaic efficiency to NH_3 – error estimation

Since it is very difficult to prepare hollow fiber electrodes with high reproducibility, the error in faradaic efficiency measurements to ammonia was estimated based on 3 independent measurements. The error was estimated using chronoamperometry at -0,6 V vs RHE at 0 ml/min and 20 ml/min (50 mM nitrate).

Table S3. Estimation of error in faradaic efficiency to NH_3 .

Flow rate [ml/min]	Faradaic efficiency to NH_3 [%]				
	Run 1	Run 2	Run 3	average	Standard dev.
0	60.4	50.2	64.9	58.8	6.1
20	45.6	34.9	37.1	39.2	4.6
	Average				5.4

Therefore, on average, an error bar of $\pm 5.5\%$ was estimated for faradaic efficiency to ammonia

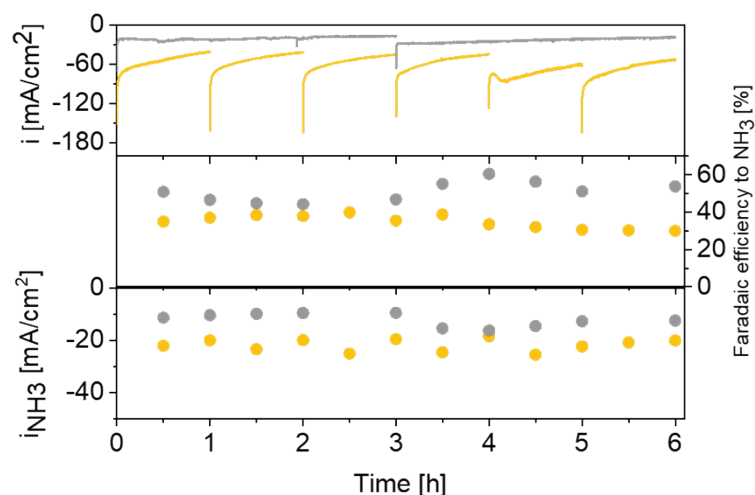


Figure S18. Stability test at -0.6 V vs RHE with 0 (gray) and 20 ml/min (yellow) flow rate showing overall current density as well as faradaic efficiency and partial current density to NH₃. (b) NH₃ mass increase in stability test in different conditions.

The partial current density to ammonia shown in Fig. 6a in main text was calculated as an average of all points measured (every 30 min). Each point was calculated using the faradaic efficiency to ammonia and the total charge passed over the period measured, thus resulting in the partial current density to ammonia reported in the main text.

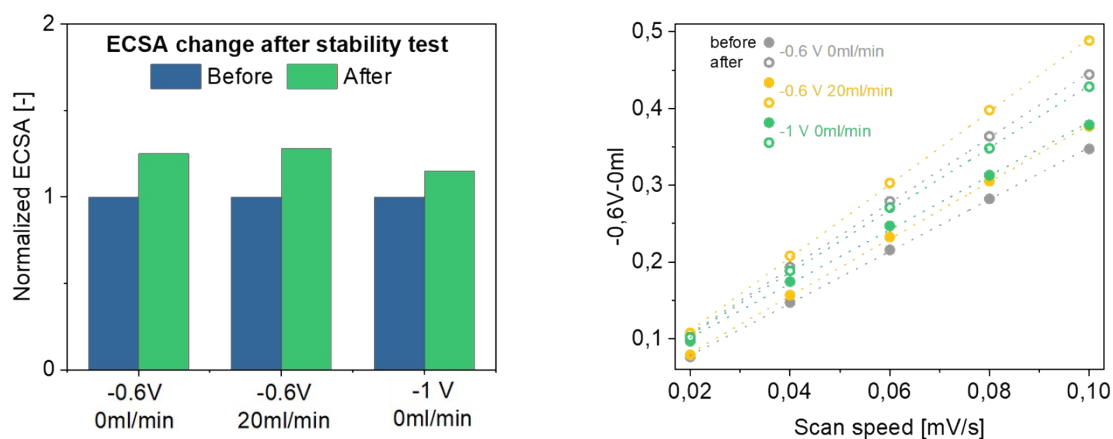


Figure S19. ECSA of Ti hollow fiber electrodes before and after stability test at different conditions.

A slight increase in surface area can be related to surface reoxidation of the Ti electrode before chronoamperometry tests. TiO_x could be reduced increasing the surface area of Ti. Additionally the formation of TiH_x could influence the ECSA.

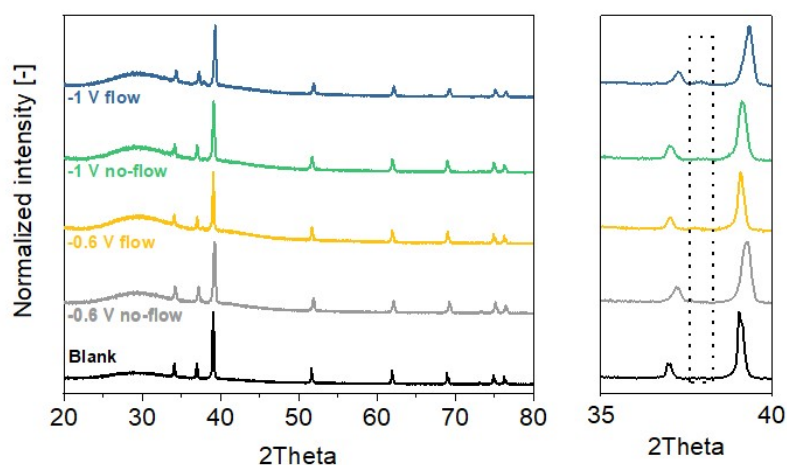


Figure S20. XRD of Ti hollow fiber electrode before and after stability test at different conditions.

A minor XRD line was observed after stability tests at -0.6 V flow, -1V no-flow, and -1V flow, which can be assigned to TiH_x formation. However, the effect is significantly lower than reported previously for Ti electrodes in the literature⁴. A broad peak in the range of 25-35 degrees is assigned to residues of the carbon tape which was used for SEM analysis prior to XRD analysis (compare XRD of Ti fiber in Figure 1d in the main text where no carbon tape was used prior to XRD analysis).

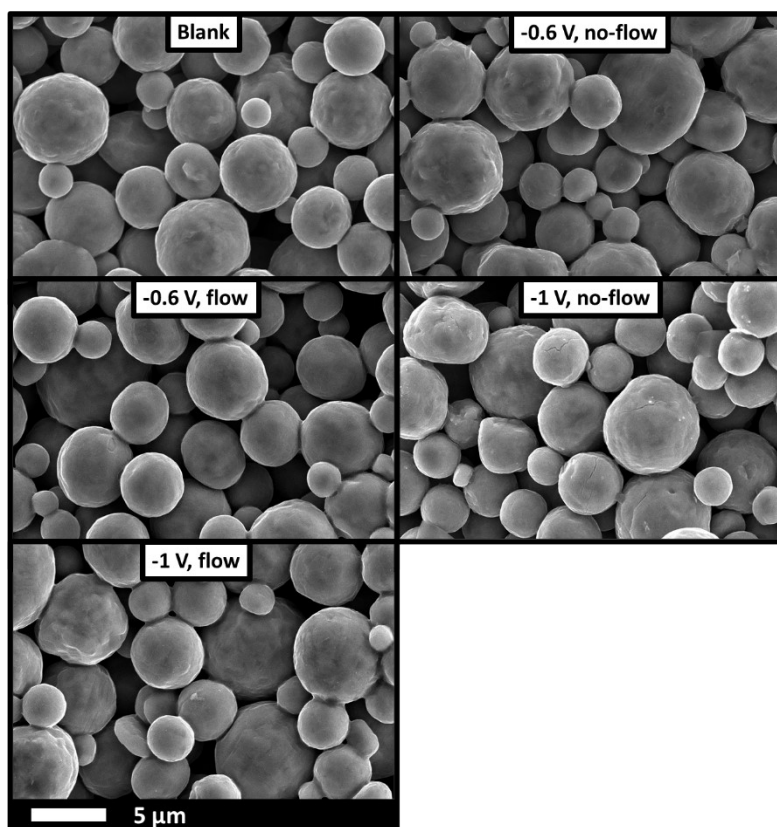


Figure S21. SEM of the Ti hollow fiber electrode before and after stability test at different conditions.

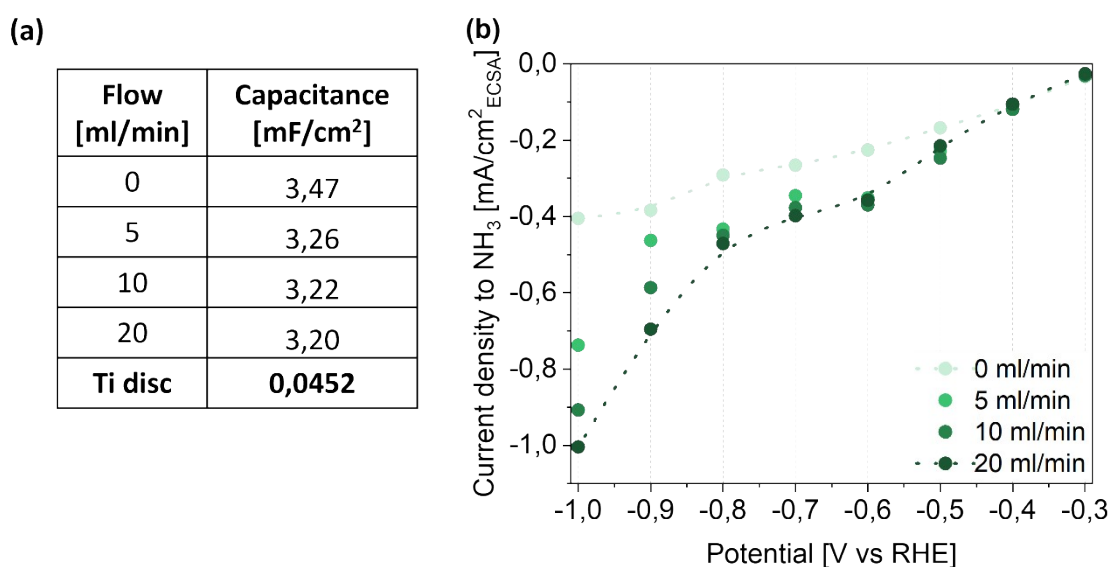


Figure S22. (a) Capacitance value for a Ti hollow fiber electrode depending on the Ar flow rate. (b) Partial current density to ammonia based on ECSA, depending on applied potential and Ar flow rate.

As shown in our previous study, the ECSA of the Ti hollow fiber electrodes can slightly change depending on the flow rate⁵. Therefore, ECSA at a specific flow rate was used for calculating the partial

current density to NH₃. Capacitance values measured at different flow rates are compared to the capacitance of a smooth Ti disc for ESCA estimation.

Table S4. Comparison of the performance of Ti-based electrodes in electroreduction of NO₃⁻.

Catalyst	Electrolyte pH	[NO ₃ ⁻]	E/i applied	i to NH ₃ [mA/cm ²]	FE [%]	ref
Ti	Neutral	100 mg/L	-20 mA/cm ²	-0.5	2.5 %	6
Ti	Neutral	50 mg/L	-38 mA/cm ²	-2.1	5.6	7
Ti	pH 3	100mg-N/L	-1.26 V vs SCE	-	~30% N-efficiency	8
TiO _{2-x}	Neutral	3.6 mM	-1.6V vs SCE	-	85	9
Ti	Acidic	0.4 M	-1 V vs RHE	-22	82	4
		50 mM	-1 V vs RHE	-4.6	<20	
Ti hollow fiber No-flow	Acidic	50 mM KNO ₃	-1 V vs RHE	~-33	58	This work*
Ti hollow fiber Flow	Acidic		-1 V vs RHE	~-75	45	This work*

*based on 4 h stability measurement

It is important to mention that not all literature reports presented in Table S4 were focused on NH₃ as a reaction product which can reflect on the data presented. Denitrification to N₂ has been the main topic so far in the nitrate electrolysis field and N₂ was the target product. Only recently ammonia is of interest which opens up the possibility for decentralized, small-scale green ammonia production plants for fertilizer applications where NO_x produced via N₂ oxidation or from waste streams can be used as feedstock.

References

- 1 A. C. Nielander, J. M. McEnaney, J. A. Schwalbe, J. G. Baker, S. J. Blair, L. Wang, J. G. Pelton, S. Z. Andersen, K. Enemark-Rasmussen, V. Čolić, S. Yang, S. F. Bent, M. Cargnello, J. Kibsgaard, P. C. K. Vesborg, I. Chorkendorff and T. F. Jaramillo, *ACS Catal.*, 2019, **9**, 5797–5802.
- 2 R. Y. Hodgetts, A. S. Kiryutin, P. Nichols, H.-L. Du, J. M. Bakker, D. R. Macfarlane and A. N. Simonov, *ACS Energy Lett.*, 2020, 736–741.
- 3 D. J. Darke, *J. Chromatogr. B*, 1980, **181**, 449–452.
- 4 J. M. McEnaney, S. J. Blair, A. C. Nielander, J. A. Schwalbe, D. M. Koshy, M. Cargnello and T. F.

- Jaramillo, *ACS Sustain. Chem. Eng.*, 2020, **8**, 2672–2681.
- 5 P. M. Krzywda, A. Paradelo, B. T. Mei, N. E. Benes and G. Mul, *ChemElectroChem*.
- 6 M. Li, C. Feng, Z. Zhang and N. Sugiura, *Electrochim. Acta*, 2009, **54**, 4600–4606.
- 7 X. Ma, M. Li, C. Feng, W. Hu, L. Wang and X. Liu, *J. Electroanal. Chem.*, 2016, **782**, 270–277.
- 8 J. Yao, Y. Mei, T. Yuan, J. Chen, H. Pan and J. Wang, *J. Electroanal. Chem.*, 2021, **882**, 115019.
- 9 R. Jia, Y. Wang, C. Wang, Y. Ling, Y. Yu and B. Zhang, *ACS Catal.*, 2020, **10**, 3533–3540.